JACS
JOURNAL OF THE AMERICAN CHEMICAL SOCIETY
Article
pubs.acs.org/JACS

Oxidation-Induced Self-Assembly of Ag Nanoshells into Transparent and Opaque Ag Hydrogels and Aerogels

Xiaonan Gao, Richard J Esteves, Thi Thu Hien Luong, Rajendra Jaini, and Indika U. Arachchige*

Department of Chemistry, Virginia Commonwealth University, Richmond, Virginia 23284-2006, United States

Supporting Information

ABSTRACT: The synthesis of hollow Ag nanoshells (NSs) with tunable plasmon bands in the visible spectrum and their oxidative-assembly into high-surface-area, mesoporous, transparent, and opaque Ag gel frameworks is reported. Thiolate-coated Ag NSs with varying size and shell thickness were prepared by fast chemical reduction of preformed Ag_2O nanoparticles (NPs). These NSs were assembled into monolithic Ag hydrogels via oxidative removal of the surface thiolates, followed by CO_2 supercritical drying to produce metallic Ag aerogels. The gelation kinetics have been controlled by tuning the oxidant/thiolate molar ratio (X) that governs the rate of NP condensation, which in turn determines the morphology, optical transparency, opacity, surface area, and porosity of the resultant gel frameworks. The monolithic Ag hydrogels prepared using high concentration of oxidant ($X > 7.7$) leads to oxidative etching of precursor colloids into significantly smaller NPs (3.2−7.6 nm), which appeared to eliminate the visible light scattering yielding transparent gel materials. In contrast, the opaque Ag aerogels composed entirely of hollow NSs exhibit enormously high surface areas (45−160 m^2/g), interconnected meso-to-macro-pore network that can be tuned by varying the inner cavity of Ag colloids, and accessibility of chemical species to both inner and outer surface of the hollows, offering perspectives for a number of new technologies. An advantage of current synthesis is the ability to transform Ag NSs into monolithic hydrogels within 4−12 h, which otherwise is reported to require weeks to months for the oxidation-induced metallic gel synthesis reported to date.

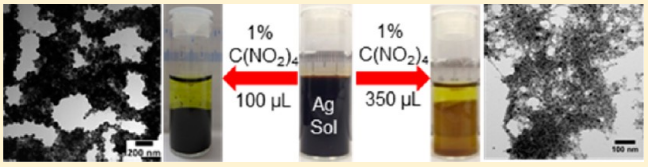

INTRODUCTION

The advent of nanotechnology has sparked many research forefronts in the creation of nanoscale materials with control over size, shape, composition, and surface properties.[1−3] However, the development of revolutionary technologies is predicated on our ability to build, orient, and assemble nanosized solids into functional architectures with useful and controllable physical properties. Numerous efforts on the assembly of nanoscale materials have been reported to date.[4−10] Recently, a proof-of-concept in which monodisperse nanoparticles (NPs) of inorganic solids can be self-organized into highly ordered superlattices through controlled evaporation of the solvent has received considerable interest.[4−7] In a number of other reports, the organic functionalities of the NP surface groups, polymers, and biomolecules have been successfully utilized to effect cross-linking of particles into one-, two-, or three-dimensional superstructures.[11−13] However, from a device performance perspective, the interactions between nanosized units are essentially mediated by organic transformations, the presence of which is detrimental to charge transport properties and limits the thermal stability of the assembly.

Aerogels, which have been rapidly developed over the past three decades, have caused great interest because of their low densities, large open interconnected pores, and high internal surface areas.[14] Such features result in potential applications as catalysts, sensors, thermal insulators, and novel electrochemical device components.[1−3,15−19] To date, a great deal of research has been conducted on aerogels based on metal oxides; among the traditional SiO_2, Al_2O_3, and TiO_2 are the widely studied systems.[14] Recently, the carbothermal reduction of metal oxide−organic polymer composites has been successfully utilized to produce Fe, Co, Ni, Sn, and Cu metallic gel frameworks.[20−22] Moreover, the extension of sol−gel chemistry to produce metal chalcogenide,[23−28] pnictide,[29] and noble metal[30,31] aerogels has been realized through the oxidation-induced self-assembly of preformed NPs. The gel frameworks composed entirely of NP colloids represent an emerging class of low-density, high-surface-area conducting superstructures in which the nanosized units are directly assembled into a pearl-necklace architectural model of the base-catalyzed silica aerogels, without the use of intervening ligands or substrate supports that can limit the charge transport and thermal stability. Nonetheless, the construction of such assemblies has been limited to solid NP constituents, hindering opportunities to develop novel superstructures with unique and potentially tunable morphologies and physical properties.

Nanomaterials with hollow interiors have received significant interest from the scientific community because of their distinct physical properties that can be tuned by engineering the size, shape, composition, and shell thickness.[32] In particular, hollow

Received: March 5, 2014
Published: May 12, 2014

   dx.doi.org/10.1021/ja5020037 | J. Am. Chem. Soc. 2014, 136, 7993−8002

NSs of Au and Ag metals exhibit plasmonic and catalytic properties either very different from or in some cases superior to corresponding solid counterparts. Zhang et al. has demonstrated that the surface plasmon resonance (SPR) of hollow Au particles can be tuned over a wide spectral region (550−820 nm) by controlling the outer diameter and shell thickness.[33,34] Such tunability of plasmonics has also been reported for silica-core/Ag-shell nanostructures.[35] Moreover, it is known that the NP morphology plays a crucial role in catalysis and the hollow NSs of noble metals supported on porous substrates have been shown exhibit superior catalytic activity in comparison to their solid counterparts.[36−40] However, the assembly of such nanocatalysts into high-surface-area, self-supported gel frameworks composed entirely of hollow particles has not been reported to date. Recently, Eychmüller et al. demonstrated the cyclodextrin-mediated self-assembly of Pt NPs into Pt aerogels.[31] Very recently, our group reported the synthesis of Au/Ag, Pt/Ag, and Pd/Ag alloy aerogels via salt-mediated cross-linking of negatively charged precursor hollows.[41] Despite recent reports on the synthesis of monometallic (Au, Ag, and Pt) and heterogeneous bimetallic (Ag−Pt and Ag−Au) solid NP-based aerogels,[30] the construction of such frameworks composed entirely of metal hollows has not been reported.

In this contribution, we report the synthesis of hollow Ag NSs displaying size and shell thickness tunable plasmonics without the use of dielectric cores such as silica beads. Moreover, for the first time we demonstrate the extension of oxidation-induced NP condensation strategy for the assembly of Ag hollows into high-surface-area, uniquely porous, transparent and opaque Ag gel frameworks. The opaque Ag aerogels, composed entirely of hollow NSs, exhibit enormously high surface areas (up to ∼160 m^2/g), extremely low densities (0.037−0.041 g/cm^3), and are morphologically similar to traditional base-catalyzed silica aerogels. As-prepared Ag aerogels demonstrate mesoporosity that can be tuned by varying the hollow cavity of the precursor particles and the accessibility of chemical species to both inner and outer surface of the hollows, offering new perspectives for a number of technologies. A unique advantage of current synthesis is the incredibly fast sol−gel transformation kinetics achieved, which otherwise is an inherently slow process for the oxidation-induced metal gel synthesis reported to date.[30]

EXPERIMENTAL SECTION

Materials. Silver nitrate (99.9%) and sodium borohydride (98%) were purchased from Strem Chemicals. Tetranitromethane and L-glutathione reduced (98%) were purchased from Sigma-Aldrich. Sodium hydroxide (ACS grade) and acetone (ACS grade) were purchased from Fisher. The water used in all syntheses was 18 MΩ milli-Q filtered. All chemicals were used as received without further purification.

Synthesis of Ag NSs. Ag NSs with varying size and shell thickness were prepared by following a literature method[42] with further modification for the purpose of large scale production (Table 1). In a typical synthesis, 50 mL of water was added to a 250 mL reaction flask in ice water bath and appropriate volumes of 10 mM $AgNO_3$ and glutathione were added (Table 1). After the reaction mixture was stirred for 5 min, its pH was adjusted to 12 using 0.1 M NaOH, which caused an immediate color change from colorless to pale yellow indicating the formation of Ag_2O NPs. Finally, an excess of $NaBH_4$ (Table 1) was swiftly injected, and the solution turned to orange-brown, pink, or purple indicating the formation of hollow Ag NSs with varying size and shell thickness. These reactions were performed multiple times to prepare 375 μmol of Ag NS solution (∼800−2400 mL) for the subsequent gelation studies.

Table 1. Volumes of 0.1 M $AgNO_3$, 10 mM glutathione, 0.1 M NaOH, and 10 mM $NaBH_4$ Used in the Synthesis of Ag NSs

sample	Plasmon band maxima (nm)	10 mM $AgNO_3$ (mL)	10 mM glutathione (mL)	0.1 M NaOH (mL)	10 mM $NaBH_4$ (mL)
1	470	3.00	0.27	10.00	3.60
2	480	3.00	0.30	10.00	3.60
3	490	3.00	0.35	10.00	3.60
4	500	1.20	0.10	10.00	3.60
5	510	1.10	0.10	10.00	3.60
6	520	1.00	0.10	10.00	3.60
7	550	1.00	0.13	10.00	3.60
8	570	1.00	0.15	10.00	3.60

Preparation of Concentrated Colloidal Sols. For the preparation of concentrated Ag sols, two techniques were employed; centrifuge filtration (CF) and rotatory evaporation (RE). With CF technique, Sartorius Vivaspin centrifuge filters (MWCO 30,000) were employed. In a typical synthesis, the centrifuge filters were filled with 20 mL of the as-prepared Ag sol, followed by centrifugation at 3000 g for 6−7 min to remove 15 mL of water and the majority of ionic byproducts (Na^+, NO_3^-, OH^-, unreacted thiolates). When the total volume was reduced to 50 mL, an aliquot of ultrapure water (200 mL) was added to wash off the remaining byproducts. After washing twice, the final volume was further reduced to 10 mL, and 0.0375 M Ag NS sol was produced (based on the moles of $AgNO_3$ used in the synthesis and assuming 100% reduction). In the case of the RE technique, 800 mL of Ag sol was first concentrated by employing centrifuge filters (∼400 mL) and then transferred to a rotary-evaporation flask. The volume was finally reduced from ∼400 to 10 mL via rotary-evaporation without disturbing the colloidal stability of the Ag NSs.

Formation of Ag Hydrogels and Aerogels. The 10 mL sol was divided into 1 mL aliquots and kept in small glass vials for the gel formation studies. For the formation of opaque Ag hydrogels, 100 μL of 1% tetranitromethane ($C(NO_2)_4$) in acetone was added to each glass vial containing 1 mL of Ag sol. The resulting mixture was vigorously shaken and left in the dark for gel formation. For the formation of transparent Ag hydrogels, 350 μL of 1% $C(NO_2)_4$ was added to each glass vial containing 1 mL of Ag NS sol. In both cases, the gradual condensation of the Ag colloids into monolithic hydrogels was observed within 4−12 h. In addition, different volumes of 1% H_2O_2 (50−500 μL) were also employed in the gel formation studies. However, with 1% H_2O_2, formation of Ag films or mirrors were observed after 4−8 weeks.

The resulting hydrogels were first washed with ultrapure water and then with acetone to remove byproducts of the oxidation. Specifically, the water layer on the top of the Ag hydrogels was removed and the acetone was carefully added along the side wall of the glass vial without breaking the Ag monolith. This process was repeated every 2 h until the pale yellow color (due to *in situ* generated HNO_3 acid) of the supernatant disappears, which is about 6−8 times washing. For the preparation of Ag aerogels, CO_2 supercritical drying (SCD) was employed. In a typical drying process, the acetone exchanged Ag wet-gels were loaded into the supercritical dryer and exchanged with liquid CO_2 4−5 times over 12−16 h at 15 °C. Finally, the temperature was raised to 40 °C and the wet-gels were dried under supercritical conditions for 20−30 min. As a comparable study, Ag xerogels were also prepared by evaporation of the solvent from acetone-exchanged wet-gels over 2−3 days.

Characterization. The powder X-ray diffraction (PXRD) patterns of the Ag samples were acquired on a Philips X'Pert X-ray diffractometer equipped with Cu Kα radiation source. The crystallite sizes were determined by applying the Scherrer formula to all diffraction peaks.[43] The solution absorption spectra of Ag NSs were recorded using a Cary 6000i UV−vis−NIR spectrophotometer. The

dx.doi.org/10.1021/ja5020037 | J. Am. Chem. Soc. 2014, 136, 7993−8002

elemental compositions of the samples were obtained from an *in situ* energy-dispersive X-ray spectroscopy (EDS) unit fitted with a Hitachi SU-70 scanning electron microscope (SEM). X-ray photoelectron spectra (XPS) were recorded using a ThermoFisher ESCALab 250 instrument equipped with a monochromated Al Kα X-ray source. The electron micrographs of the samples were recorded using a JEOL JEM-1230 transmission electron microscope equipped with a Gatan ultrascan 4000 camera operating at an accelerating voltage of 120 kV. The NS samples were prepared by depositing a drop of Ag sol onto the carbon-coated copper grid, followed by ambient evaporation of the solvent. The aerogel samples were prepared on copper grids by dispersing fine powders in acetone via sonication and depositing a drop of suspension onto the copper grid, followed by evaporation of the solvent. The N_2 adsorption/desorption isotherms were acquired using a Micromeritics ASAP 2020 surface area and porosimetry analyzer at 77 K. All samples were degassed under vacuum at 50 °C for 24 h prior to the analysis. The isotherm data were fit using the Brunauer–Emmett–Teller (BET) model to calculate the surface area values. The average pore diameters and cumulative pore volumes were obtained by applying the Barrett–Joyner–Halenda (BJH) model to desorption branches of the respective isotherms. Five independently prepared samples were analyzed for each system.

RESULTS AND DISSCUSSION

The size and shell thickness tunable Ag NSs were prepared by fast chemical reduction of preformed Ag_2O NPs. The precursor Ag_2O templates were produced by the reaction of $AgNO_3$ with NaOH in the presence of glutathione surfactant. Following the synthesis of the Ag_2O, an aqueous solution of $NaBH_4$ was quickly injected under vigorous stirring, which caused an immediate color change from pale-yellow to orange-brown, pink, or purple indicating the reduction of Ag_2O into hollow Ag nanostructures. This fast reduction step is found to be critical for the formation of narrowly disperse Ag NSs with uniform size and shell thickness. In contrast, when the reduction reactions were performed with the slow addition of $NaBH_4$ (0.5 mL/min.) significantly smaller solid NPs (4–6 nm) were produced (Supporting Information, Figure S1). It has been proposed that the transformation of Ag_2O into hollow Ag NSs is triggered by the slow inward diffusion of $NaBH_4$ and rapid outward diffusion and dissolution of Ag^+ via a nanoscale Kirkendall-type reaction.[42] However, in the above report the synthesis of single crystalline Ag NSs with plasmon band centered at 480 nm is reported and the facile tunability of the NS size and shell thickness has not been reported. In a recent study, synthesis of Ag hollows with SPR maxima in the range of 455–605 nm is demonstrated by varying the nature and concentration of the reducing agent and the thiolate surfactant.[44] However, significantly broad plasmonic bands (full with at half maxima, fwhm = 140–550 nm) were attained owing to poor size and shell thickness control, which is also apparent in the TEM images.[44] Nonetheless, we found that the outer diameter and shell thickness of the Ag NSs can be tuned by varying the concentration of $AgNO_3$ and thiolates in the reducing mixture and consequently the size of the sacrificial Ag_2O template. This has been achieved through fine-tuning the molar ratio of $AgNO_3$ to glutathione while keeping the moles of NaOH and $NaBH_4$ constant under ambient conditions. As-prepared Ag NSs display a progression in color from orange-brown to pink or purple as the SPR bands are red-shifted with increasing size and shell thickness (Figure 1). The fwhm of the plasmonic bands were in the range of 58–121 nm, indicating the narrow dispersity of as-prepared samples. In contrast, the solid Ag NPs produced via slow addition of $NaBH_4$ exhibit a SPR maximum at 410 nm (Supporting Information, Figure S1).

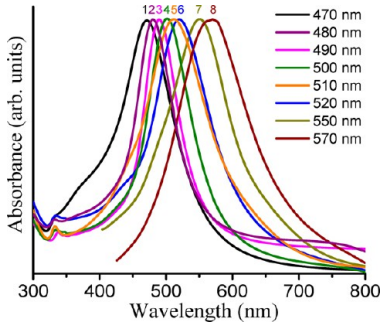

Figure 1. Normalized UV–vis absorption spectra of the as-prepared Ag hollow NSs (sample 1 through 8) displaying surface plasmon resonance maxima at (1) 470, (2) 480, (3) 490, (4) 500, (5) 510, (6) 520, (7) 550, and (8) 570 nm.

The red shift observed in the SPR for Ag NSs is consistent with previous reports on hollow Au NSs where a similar shift is observed with increasing size and shell thickness.[33,34] The TEM images of the NSs show that in all samples large hollows have been created (Figure 2). The elemental compositions, wavelengths of the SPR maxima, crystallite sizes, shell thicknesses, inner and outer diameters, surface areas, and porosities of the selected Ag NSs used in the metallic gel synthesis are reported in Table 2.

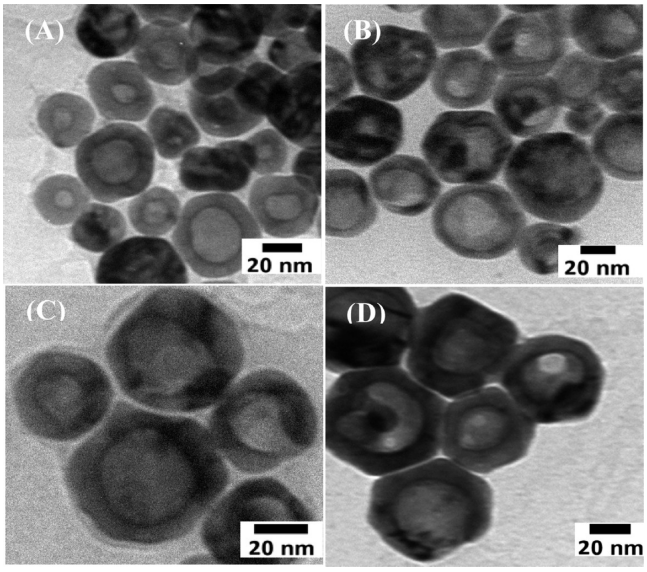

Figure 2. Transmission electron micrographs of the Ag hollow NSs displaying (A) 24.1 ± 4.5, (B) 46.2 ± 5.4, (C) 55.1 ± 6.5, and (D) 60.1 ± 7.6 nm average outer diameters.

For the Ag gel synthesis, we have specifically investigated the use of 24.1 ± 4.5, 46.2 ± 5.4, 55.1 ± 6.5, and 60.1 ± 7.6 nm outer diameter Ag NSs representing a wide range of NS sizes and shell thicknesses, which are designated as NS I, NS II, NS III, and NS IV, respectively. Corresponding aerogel products are termed as AG I, AG II, AG III, and AG IV, respectively (Table 2). In general, the sol–gel transformation of NP colloids requires highly concentrated sols that can be placed in suitable conditions for the self-assembly.[28] Typically, the destabilization of NP sol leading to controlled aggregation is achieved by oxidative removal of the surfactant ligands.[28] It was found that the glutathione functionality provides the highest colloidal stability of Ag NSs as well as efficient destabilization through

dx.doi.org/10.1021/ja5020037 | J. Am. Chem. Soc. 2014, 136, 7993–8002

Table 2. Comparison of Crystallite Sizes, Average Shell Thicknesses, Inner and Outer Diameters, Elemental Compositions, Wavelengths of the SPR Maxima, Surface Areas, Average Pore Diameters, and Cumulative Pore Volumes of the As-Prepared Ag NSs (NS I–IV) and the Corresponding Aerogels (AG I–IV) along with the Densities of Ag Aerogels

	nanoshells				aerogel			
sample	NS I	NS II	NS III	NS IV	AG I	AG II	AG III	AG IV
Crystallite size (nm)[a]	16.5 ± 0.2	19.6 ± 0.2	22.5 ± 0.2	25.1 ± 0.2	12.3 ± 0.2	17.6 ± 0.2	19.5 ± 0.2	N/A
shell thickness (nm)[b]	5.8 ± 0.9	9.1 ± 1.2	10.4 ± 1.4	11.2 ± 1.8	5.5 ± 0.9	8.9 ± 1.2	10.1 ± 1.6	N/A
inner diameter (nm)	12.5 ± 3.1	28.1 ± 4.8	34.3 ± 5.2	37.7 ± 6.8	11.8 ± 1.5	25.9 ± 2.1	33.1 ± 2.8	N/A
outer diameter (nm)	24.1 ± 4.5	46.2 ± 5.4	55.1 ± 6.5	60.1 ± 7.6	22.8 ± 1.9	43.7 ± 3.0	53.3 ± 3.5	N/A
composition[c]	Ag 86.34%	Ag 85.06%	Ag 84.25%	Ag 83.48%	Ag 95.43%	Ag 96.14%	Ag 95.55%	Ag 96.40%
	S 13.66%	S 14.94%	S 15.75%	S 16.52%	S 4.57%	S 3.85%	S 4.45%	S 3.60%
SPR maxima (nm)	480	500	510	520	N/A	N/A	N/A	N/A
density (g/cm^3)	N/A	N/A	N/A	N/A	0.041	0.037	0.038	0.04
surface area (m^2/g)[d]	7.6	6.2	3.1	4.9	127–160	81–98	76–127	43–46
molar surface area (m^2/mol)[e]	820.8	669.6	334.8	531.2	1.4–1.7 × 10^4	0.87–1.1 × 10^4	0.83–1.4 × 10^4	4.7–4.9 × 10^3
cumulative pore volume (cm^3/g)	0.021	0.038	0.026	0.027	0.53–0.73	0.28–0.86	0.33–1.12	0.28–0.33
average pore width (nm)[f]	5.2	15.6	12.1	16.6	10.3–17.2	12.8–21.5	20.9–21.3	19.8–21.1

[a]The Scherrer analysis was employed to calculate the crystallite size using all diffraction peaks in the powder pattern. [b]Average nanoshell thicknesses were obtained by calculating the inner and outer diameter of 100–200 nanoshells from TEM images. [c]SEM/EDS analysis was used to obtain the elemental composition of multiple samples, and the average values are presented. [d]Surface area values were obtained by applying the BET model to nitrogen adsorption/desorption isotherms. [e]Molar surface area values were calculated by multiplying the BET surface area by the molar mass of metallic Ag. [f]The BJH model was applied to the desorption branches of the respective isotherms to calculate the average pore diameters and cumulative pore volumes.

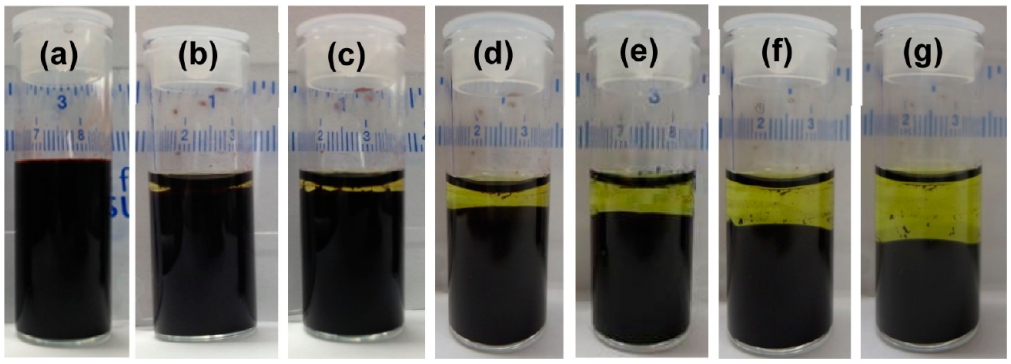

Figure 3. Photographs illustrating the transformation of Ag NS sol into an opaque gel and the compaction and syneresis that occurs upon gel aging: (a) concentered Ag sol, Ag sol (b) 1 h and (c) 1.5 h after the addition of $C(NO_2)_4$, gel aged for (d) 2 h, (e) 2.5 h, (f) 3.5 h, (g) 5 h. The oxidant/thiolate (X) ratio is 2.2 and the bottom scale bar is in centimeters.

oxidation as it can strongly complex with the surface Ag and the solvent water molecules. Hence, highly concentrated Ag colloids (0.03–0.05 M) coated with glutathione were prepared by using either the RE or the CF technique.

Initially, we have investigated the synthesis of Ag hydrogels using common oxidants and the concentrated colloids produced by RE technique. The introduction of $C(NO_2)_4$ or H_2O_2 into Ag sols (obtained from rotary evaporation) did not produce corresponding hydrogels; however thin sheet-like Ag films were obtained after 1–2 months. It is likely that the ionic byproducts (Na^+, NO_3^-, OH^-) present in the concentrated Ag sols can reduce the stability of NSs resulting in precipitation, followed by decomposition into Ag films. Hence, the purification of Ag colloids prior to the application of oxidant is found to be essential for the successful assembly of NSs. In contrast, CF technique offers an effective method to produce purified Ag colloids via removal of solvated ions along with excess water while retaining the colloidal stability of Ag NSs. Consistent with our hypothesis, monolithic Ag hydrogels were produced after the addition of $C(NO_2)_4$ into concentrated Ag sols obtained from CF technique. Nonetheless, attempts to produce Ag gels using H_2O_2 and purified colloids obtained from CF technique were not successful owing to rapid oxidation of glutathione, followed by precipitation of Ag NSs.[45] Conversely, the progressive removal of glutathione was only achieved by employing different volumes (50–500 μL) of 1% $C(NO_2)_4$. The addition of $C(NO_2)_4$ results in the slow oxidation of thiolates into disulfides as the primary byproduct (eq 1 and 2),[46] creating active sites on the NS surface. Consequently, these active sites can undergo direct cross-linking to produce monolithic Ag hydrogels (Figure 3).

$$GSH + C(NO_2)_4 \rightarrow GSNO_2 + C(NO_2)_3^- + H^+ \quad (1)$$

$$GSH + GSNO_2 \rightarrow GS - SG + NO_2^- + H^+ \quad (2)$$

$$3HNO_2 \rightarrow 2NO + HNO_3 + H_2O \quad (3)$$

It was also revealed that the ability to transform Ag colloids into a nanoparticulate gel material relies in part on the kinetics by which active sites for the assembly become available on the

dx.doi.org/10.1021/ja5020037 | J. Am. Chem. Soc. 2014, 136, 7993–8002

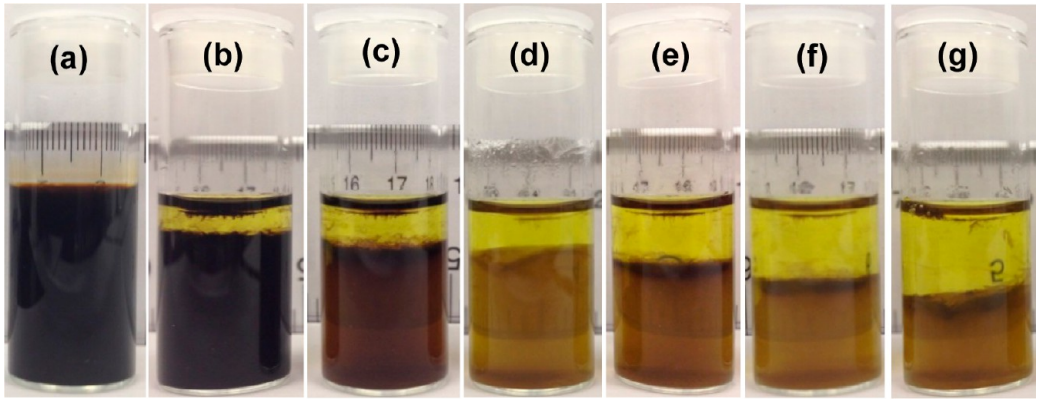

Figure 4. Photographs showing the condensation of opaque Ag sol into transparent Ag hydrogel: (a) concentrated Ag sol; (b) sol 2 h after treatment with $C(NO_2)_4$, gel aged for (c) 4 h, (d) 6 h, (e) 8 h, (f) 10 h, and (g) 12 h. The oxidant/thiolate molar ratio (X) is 7.7.

NS surface. If no sites are available because of the strict passivation by glutathione, Ag colloids are stable in solution, whereas if too many sites become available at one time, rapid precipitation can occur. Therefore, the gelation kinetics can be tuned by varying the quantity of the oxidant relative to the amount of thiolate (glutathione) present in the solution. Accordingly, we found that up to a minimum molar ratio of oxidant/thiolate, X_{min} = 1.1, Ag colloids are highly stable in solution and the gelation is not observed. Above X_{min}, the rapidity at which gel formation occurs increases with increasing X, until the kinetics are so fast that a precipitate forms in lieu of a gel at X = 13.2 (i.e., $12X_{min}$). At high concentrations of $C(NO_2)_4$, the large number of active sites facilitates the interparticle cross-linking, resulting in more compact Ag hydrogels. Likewise, significant polymerization during the gel aging results in dense hydrogels. Therefore, as a preliminary investigation, the gelation was studied with different molar ratios of oxidant/thiolate. We found that the X = 1.65 provides the optimum conditions to produce opaque Ag hydrogels retaining the precursor NS morphology, high surface area, and porosities. Thereafter, opaque Ag hydrogels were produced primarily with X = 1.65. Interestingly, when X > 7.7 yellow-brown colored transparent Ag hydrogels were obtained (Figure 4). Notably, the transparent hydrogels experienced a much slower condensation rate in comparison to opaque Ag hydrogels. As-synthesized Ag hydrogels were aged under ambient conditions for 6−8 h and the byproducts of the oxidation (disulfides and sulfonates) were removed by exchanging the solvent 6−8 times with acetone over 1−2 days. Finally, the acetone-exchanged wet gels were dried using supercritical CO_2 to produce monolithic Ag aerogels.

As-prepared Ag aerogels were black (opaque hydrogels) or brownish-black (transparent hydrogels) in color and showed a 5−10% volume loss when compared to acetone-exchanged wet-gels. Interestingly, the monoliths of Ag aerogels exhibit densities as little as 0.037−0.041 g/cm^3, representing ∼0.4% of the density of bulk Ag. This study offers a novel approach for the construction of metal aerogels with control over physical properties through fine-tuning the oxidant/thiolate molar ratio, providing great advantage over previously reported metal NP condensation strategies,[30] which appeared to lack such control over gelation kinetics.

The oxidative removal of the glutathione ligands from Ag NSs and subsequent SCD drying has no apparent impact on the structure and crystallinity of the Ag NSs that make up the gel framework (Figure 5). The X-ray diffraction patterns of the

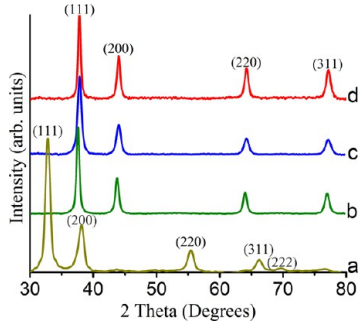

Figure 5. Powder X-ray diffraction patterns of the cubic Ag_2O NPs (a) along with the 24.5 ± 4.5 nm outer diameter cubic Ag NSs (b) produced from Ag_2O templates. PXRD patterns of the corresponding Ag aerogels (c) and xerogels (d) produced via oxidative-assembly of Ag NSs.

Ag aerogels and xerogels are characteristic of the cubic Ag phase (PDF No. 01-0870-719) with broadening of Bragg reflections owing to nanoparticulate nature of the material. The diffraction peaks corresponding to precursor Ag_2O (PDF No. 43-997) were not observed in the powder patterns of Ag hollows and corresponding gel products indicating the successful reduction of Ag_2O to metallic silver. Average crystallite sizes estimated based on Scherrer analysis suggest that the Ag crystallites within the gel frameworks are slightly smaller than those of precursor NSs, which is consistent with the TEM measurements (Table 2). This can be attributed to oxidative etching of the Ag hollows by $C(NO_2)_4$ and the HNO_3 acid byproducts during self-assembly, which has been proven to reduce the size of Ag particles.[47,48] Nevertheless, the core crystal structure remains unchanged upon gelation and subsequent aero-/xero-gel formation.

The elemental compositions of the precursor NSs and aerogels were investigated by employing the SEM/EDS on several individually prepared samples, and the average results are shown in Table 2. The precursor NSs prepared by the reduction of Ag_2O exhibit two prominent peaks in the EDS spectrum corresponding to Ag and S with atomic ratios in the range of 83−86%:17−14% (Figure S2, Supporting Information). In addition, peaks corresponding to oxygen and carbon are also observed in the Ag NSs, which can be attributed to surface bound glutathione ligands. Upon gelation and aerogel formation, no peak for oxygen is detected indicating the successful reduction of Ag_2O to metallic Ag and the removal of

dx.doi.org/10.1021/ja5020037 | J. Am. Chem. Soc. 2014, 136, 7993−8002

glutathione during the precursor NS synthesis and oxidation-induced self-assembly, respectively. Moreover, the S content is dramatically reduced to 3−5% in the aerogel product, which further confirms the oxidative removal of glutathione (Table 2). As described earlier, Ag hydrogels can also be prepared by varying the oxidant/thiolate molar ratio (X value) in the concentrated colloidal solutions. Using the above phenomena oxidative removal of glutathione can be further established by the fact that the atomic percentage of the S decreases as 5.5, 4.7, 4.1, 2.8, and 2.1% in the corresponding aerogel product when the oxidant/thiolate molar ratio (X) is systematically increased from 1.1, 1.7, 2.2, 3.3, and 4.4, respectively.

To monitor the oxidation state of Ag throughout the self-assembly, XPS studies were performed on Ag NSs, corresponding opaque and transparent Ag gel materials. Ag ($3d_{5/2}$) binding energy of 367.6 eV was obtained for precursor NSs indicating nearly complete reduction of Ag_2O to metallic Ag (Figure 6A).

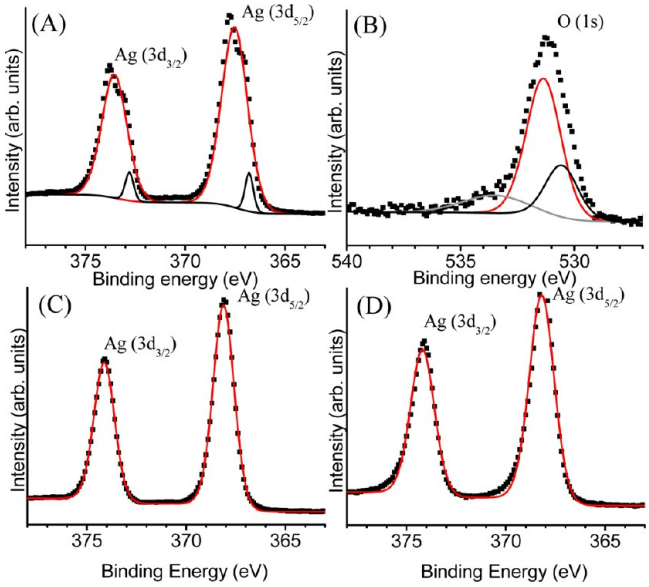

Figure 6. (A) Ag ($3d_{5/2}$) and (B) O (1s) XPS spectra of the precursor NSs along with the Ag ($3d_{5/2}$) spectra of the aerogels produced from (C) opaque and (D) transparent Ag hydrogels. The dotted lines represent spectral data. Solid black, gray, and red lines are the fitted deconvolutions.

The Ag metal exhibits a binding energy of 368.0 eV for Ag ($3d_{5/2}$),[49] the negative 0.4 shift observed can be attributed to the presence of surface Ag^+ species that are coordinated to glutathione ligands. Further, the analysis of O (1s) spectrum indicates binding energies of 530.56 and 531.35 eV for O (1s) which can be assigned to the C═O and C−O bonds of the glutathione moiety (Figure 6B). The small peak at 533.5 eV in the O (1s) spectrum is likely caused by trapped surface contaminates from exposure to ambient air. If significant Ag_2O is present in the precursor NSs, a binding energy of 529.0 eV is expected.[50] The side hump observed at 366.9 eV for Ag ($3d_{5/2}$) can be assigned to Ag−S−C surface states likely formed through coordination of glutathione.[49] Moreover, the S (2p) spectrum (Supporting Information, Figure S3) has a binding energy of 161.9 eV for S (2p), which can be assigned to the S^{2-} linking the surface Ag^+ with glutathione.[51] In contrast, significant changes in the XPS spectra were observed upon gelation and aerogel formation. In the corresponding opaque and transparent aerogels, the Ag ($3d_{5/2}$) spectra (Figure 6C,D) indicate the disappearance of the Ag−S−C species with only metallic Ag present at 368.1 eV. This observation is consistent with the removal of glutathione moiety from precursor NSs and suggests that the oxidation-induced self-assembly has no effect on the valence state of Ag and the loss of Ag^+ species is attributed to the etching effect caused by the acid by-products. Further, the examination of the S (2p) spectra of both transparent and opaque aerogels indicates the formation of additional S species, which are likely to be produced through oxidation of glutathione into disulfides and sulfonates (Supporting Information, Figure S3).[45]

Transmission (TEM) and scanning (SEM) electron microscopies were employed to investigate the morphology of Ag NSs, corresponding opaque and transparent Ag aerogels. As shown in Figure 2, precursor NSs exhibit hollow morphology with narrowly dispersed size and shell thickness, which is consistent with the tunable plasmonics observed in the visible spectrum (Figure 1). Representative SEM and TEM images of opaque aerogels are shown in Figures 7A and 8A−D, respectively. SEM images indicate the highly porous morphology of the aerogel product displaying pearl necklace aggregates of precursor particles (Figure 7A). In contrast, a larger degree of fusion and densification is observed in the benchtop dried xerogel samples (Figures 7B and 8E). Similarly, the TEM images of the aerogels assembled from NS I, NS II, and NS III particles exhibit an interconnected network of Ag hollows that

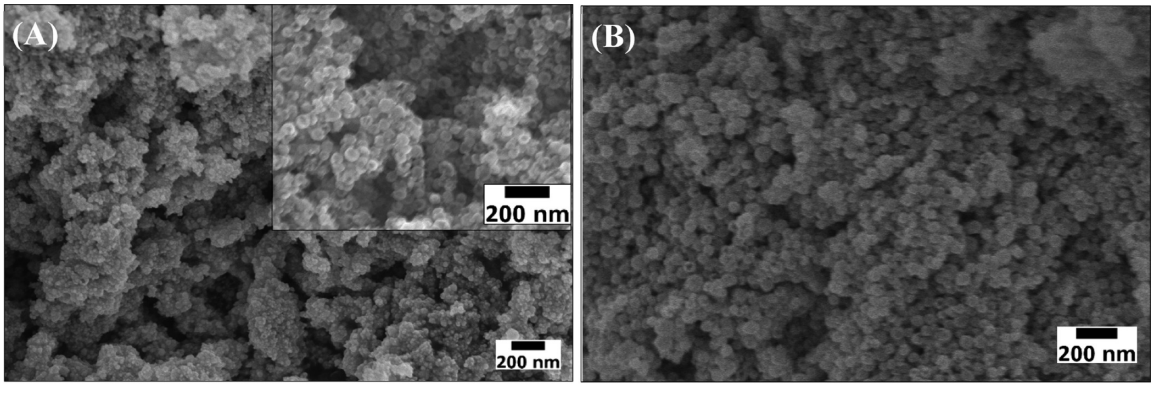

Figure 7. Representative SEM images of opaque (A) Ag aerogels and (B) xerogels assembled from 24.1 ± 4.5 nm outer diameter Ag NSs. Inset in panel A shows the high resolution SEM image depicting the interconnected network of Ag hollow particles.

dx.doi.org/10.1021/ja5020037 | J. Am. Chem. Soc. 2014, 136, 7993−8002

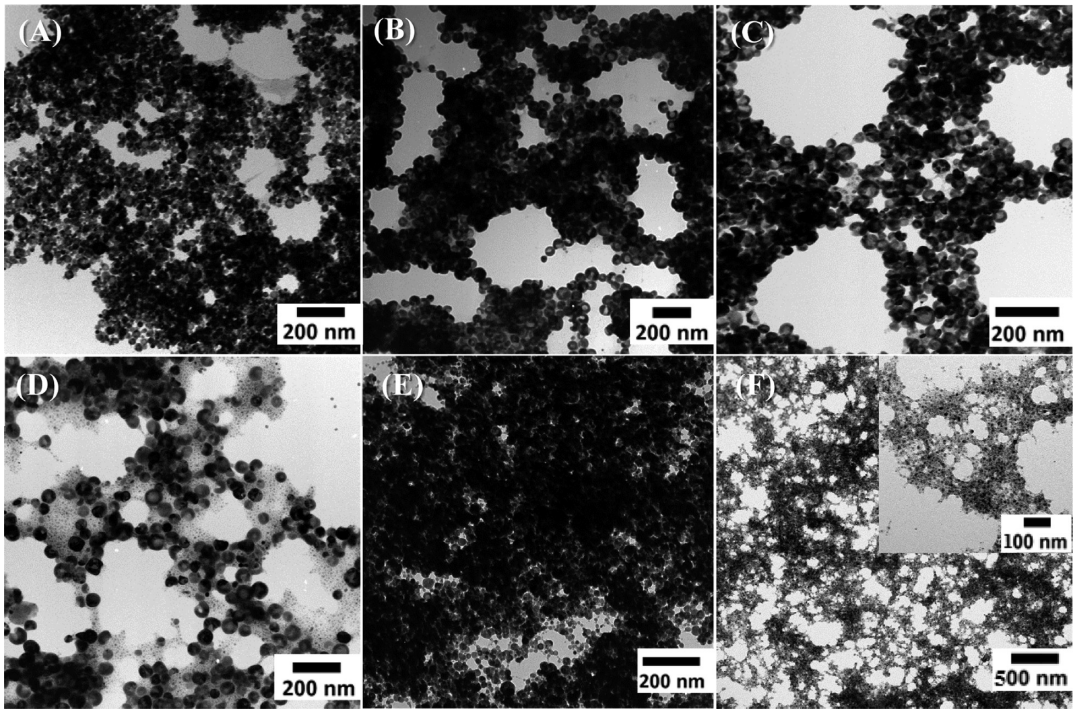

Figure 8. TEM images of the aerogels assembled from (A) 24.1 ± 4.5 nm, (B) 46.2 ± 5.4 nm, (C) 55.1 ± 6.5 nm, and (D) 60.1 ± 7.6 nm outer diameter Ag NSs. TEM images of the (E) xerogels and (F) aerogels derived from 24.1 ± 4.5 nm outer diameter NSs and transparent hydrogels, respectively. The inset in panel F shows the magnified image of the sample F. The dark contrast areas in A–F represent multiple layers of particles depicting the 3-dimensional connectivity of Ag NSs.

have typical dimensions in the same scale as precursor particles (Figure 8A–C and Figure S4, Supporting Information). Thus, the corresponding Ag aerogels (AG I–III) are likely to produce through direct cross-linking of hollow NSs into fractal aggregates and are morphologically similar to traditional base-catalyzed silica aerogels.[14] However, the gel frameworks assembled from NS IV particles exhibit significant changes in morphology (Figure 8D) in comparison to precursor NSs (Figure 2D). The AG IV product consists of an interconnected network of large Ag hollows and small NPs, which appeared to result from the breakup of the precursor NSs. The origin of small NPs can be attributed to lower stability of significantly larger hollows that can breakup into smaller NPs (6–20 nm) upon oxidation-induced self-assembly. However, the presence of a meso (2–50 nm) to macro (>50 nm) -porous network with a wide range of pore diameters is clearly visible in all aerogel samples.

As discussed above, if a large excess of oxidant is used in the self-assembly process, optically transparent Ag gel materials can be produced (Figure 4). TEM analyses of the corresponding aerogels exhibit significantly smaller (3.2–7.6 nm) NPs that are 3-dimensionally linked together to produce pearl necklace aggregates (Figure 8F and Figure S5, Supporting Information). It is likely that the precursor NSs are no longer stable as hollows in the transparent hydrogels, and hence, can breakup into significantly smaller NPs (3.2–7.6 nm) in the presence of excessive oxidant ($X > 7.7$). It was revealed that the oxidative removal of glutathione generates HNO_3 acid as a byproduct resulting in a slightly acidic Ag sol (eq 3). The in situ generated HNO_3 is likely to etch the larger Ag hollows into significantly smaller NPs yielding transparent Ag hydrogels (Figure 4). A relatively slower condensation rate observed in the formation of transparent hydrogels is likely caused by the slower etching rate of Ag by in situ generated HNO_3 acid. Previously, it has been reported that the transparent chalcogenide gel materials can be produced when the size of the NP aggregates falls below the wavelength of visible light.[23,25,52,53] Brock et al. have extensively studied the gelation kinetics of CdSe NPs and concluded that the smaller NPs can undergo reaction limited colloidal aggregation resulting in aggregates that are smaller than the wavelength of visible light, leading to optical transparency,[52] whereas, with larger NPs, the aggregates formed at the gelation point are much larger than the wavelength of visible light, resulting in increased scattering and opacity. Likewise, the Ag hydrogels assembled from larger hollows (~24–60 nm) exhibit opaque gel materials while the smaller NP building blocks (~3.2–7.6 nm) can potentially result in transparent Ag gel materials.

The low-density, highly porous structure of the metallic Ag aerogels is further reflected in the surface area and porosimetry plots modeled from the nitrogen adsorption/desorption isotherms (Figure 9). Both transparent and opaque Ag aerogels exhibit similar-shaped isotherms that can be classified as a type IV curve, characteristic of a mesoporous (2–50 nm) material with a sharp upturn in the high-relative-pressure region that corresponds to a type II curve indicating the capillary condensation and some degree of macroporosity (>50 nm).[54,55] The shapes of the hysteresis loops of all samples reveal a combination of H1 and H3 character suggesting the presence of cylindrical-shaped and slit-shaped pores, respectively.[55] The surface area calculated based on the Brunauer–Emmett–Teller (BET) model is in the range of 43–160 m^2/g (~4.7–17.2 × 10^3 m^2/mol) for opaque aerogels, whereas the aerogels produced from transparent hydrogels exhibit a slightly higher surface area (175–182 m^2/g or 18.9–19.7 × 10^3 m^2/mol), which is consistent with the significantly smaller NPs

dx.doi.org/10.1021/ja5020037 | J. Am. Chem. Soc. 2014, 136, 7993–8002

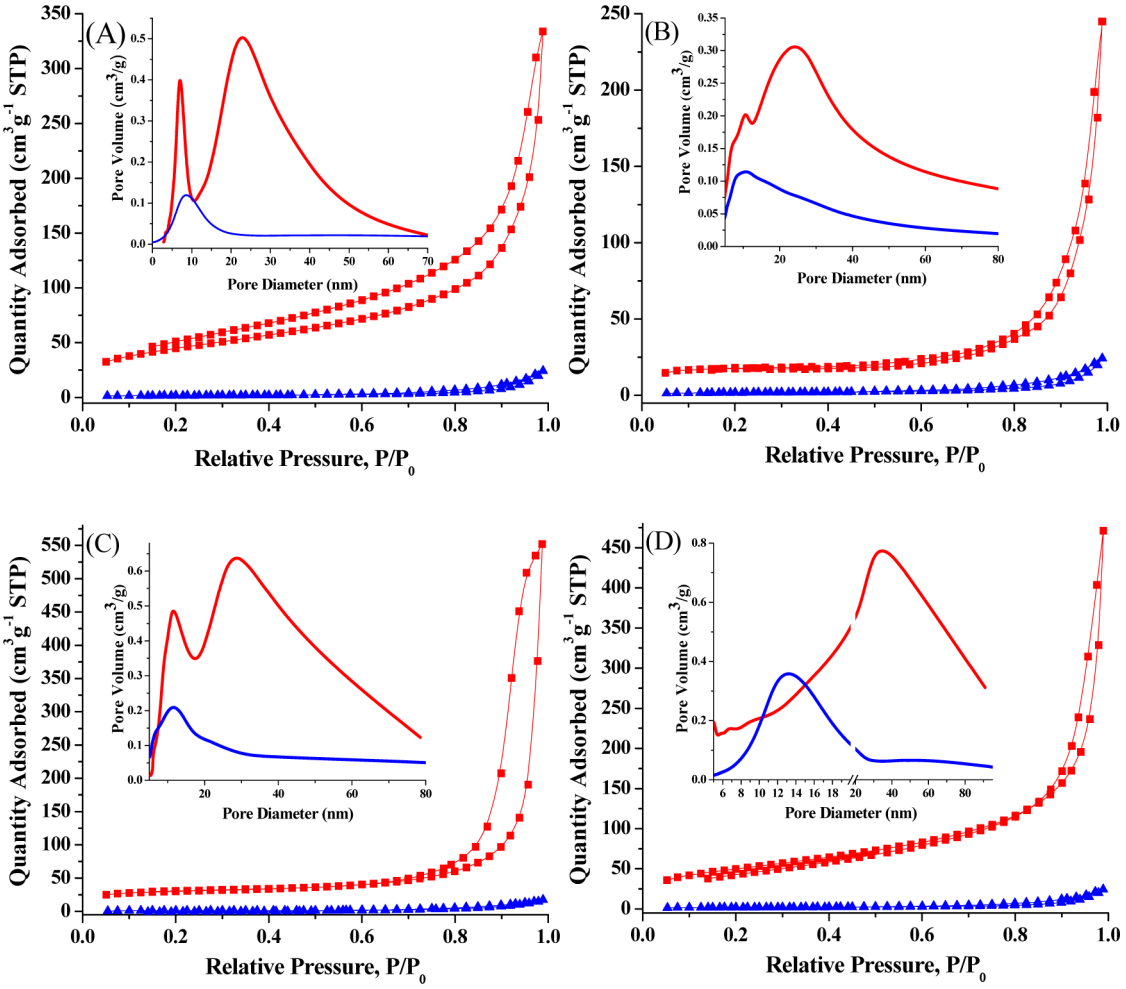

Figure 9. Nitrogen adsorption/desorption isotherms of precursor Ag NSs (blue) and corresponding aerogels (red) assembled from (A) 24.1 ± 4.5, (B) 46.2 ± 5.4, (C) 55.1 ± 6.5 nm outer diameter Ag NSs and (D) the aerogels produced from transparent hydrogels. Respective BJH pore distribution plots of Ag NSs (blue) and aerogels (red) are shown as insets.

present in the transparent Ag gel frameworks (Figure 8F). In general, a systematic decrease in surface area with increasing outer diameter and shell thickness of precursor NSs is observed for AG I through AG III samples (Table 2). In contrast, the hollow Ag NSs are significantly less porous and exhibit BET surface areas in the range of 3.1−7.6 m^2/g (~334−821 m^2/mol). The enormously high surface areas obtained for Ag aerogels in comparison to precursor NSs can be attributed to low-density highly porous architecture of the aerogel framework, which provides the superior accessibility of chemical species to inner and outer surface of the hollows, offering new perspectives for future applications.

The average pore diameters and cumulative pore volumes of the Ag aerogels were obtained from the desorption branches of the nitrogen adsorption/desorption isotherms using the Barrett−Joyner−Halenda (BJH) model. As a comparable study, pore size distribution plots of precursor NSs were also modeled using the respective isotherms. The pore distribution analyses (Figure 9A−D insets) of transparent and opaque Ag aerogels exhibit a broad range of pore sizes, extending from the meso-to-macro-pore region, yielding average diameters in the range of 10.3-21.3 nm (Table 2). Interestingly, the opaque Ag aerogels retaining the hollow morphology of precursor NSs exhibit two distinct pore distributions in the mesoporous (2−50 nm) region. For instance, the aerogels assembled from 24.1 ± 4.5 nm outer diameter NSs demonstrate a narrow pore distribution centered at ~7 nm and a much broader pore distribution ranging from 15 to 50 nm (Figure 9A inset). In contrast, precursor NSs exhibit a single pore distribution centered at ~8 nm, which is likely to arise from the hollow cavity of the particles. Accordingly, the narrow pore distribution centered at ~7 nm of the aerogel product can be attributed to the hollow interior of the precursor NSs, whereas the latter distribution reflects the continuous meso-to-macro-pore network created by the 3-dimensional assembly of Ag NSs. The relative area under those two distributions represents the contribution from each toward the cumulative pore volume, and the gel framework assembled from 24.1 ± 4.5 nm Ag NSs exhibits ~17% and ~83% contribution from NS pores and network pores, respectively. Similar pore distributions were obtained for aerogels assembled from 46.2 ± 5.4 and 55.1 ± 6.5 nm outer diameter NSs as they retain the hollow morphology of the nanosized constituents (Figure 9B,C). Therefore, unlike the traditional metal oxide or the dense NP-based gel materials, the metallic aerogels reported in this study are unique nanoarchitectures that can exhibit tunable surface areas and porosities even within a traditionally nonordered superstructure. This unique pore size tunability could in principle be useful in the selective analysis of chemical species as a function of the inner diameter of the NSs, which can potentially

dx.doi.org/10.1021/ja5020037 | J. Am. Chem. Soc. 2014, 136, 7993−8002

create customized gel frameworks for future catalytic and sensing applications. In contrast, the aerogels constructed from 60.1 ± 7.6 nm outer diameter Ag NSs (Figure S6, Supporting Information) and the transparent Ag hydrogels (Figure 9D) exhibit a single pore distribution that corresponds to network pores owing to lack of hollow particles in the corresponding gel structures.

CONCLUSIONS

We have successfully demonstrated the synthesis of size and shell thickness tunable Ag NSs and their self-supported assembly into opaque and transparent Ag gel frameworks via oxidative removal of the surface functionalities. The Ag NSs prepared by fast chemical reduction of Ag_2O exhibit narrow and tunable plasmonic bands in the visible spectrum (470−570 nm) that are significantly red-shifted from solid NP counterparts (410−420 nm). Glutathione surface functionality enables the production of highly concentrated (0.03−0.05 M) Ag sols via centrifuge filtration, whereas the introduction of $C(NO_2)_4$ induces the oxidative removal of glutathione, leading to direct cross-linking of Ag hollows into metallic Ag gel frameworks. The oxidant/thiolate molar ratio (X) determines the rate of NP condensation, which in turn determines the morphology, optical transparency, opacity, surface area, and porosity of the resultant Ag aerogels. As-prepared opaque Ag aerogels exhibit extremely low densities, high-surface-area, and porosities that can be tuned by varying the inner diameter of the precursor colloids as well as classic pearl necklace morphology of the base-catalyzed silica aerogels. The high concentration of oxidant (X > 7.7) facilitates the oxidative etching of Ag NSs into significantly smaller NPs (3.2−7.6 nm) that can result in optically transparent Ag hydrogels. While the tunable plasmonic properties of the precursor NSs are lost upon sol−gel assembly the catalytic and surface enhanced Raman scattering (SERS) activities of the nanoscale building blocks are expected to be retained in the resultant aerogel product. Hence, these low-density mesoporous nanoarchitectures displaying optical transparency or opacity, enormously high-surface-area, and interconnected meso-to-macro-pore structure would be promising candidates for catalytic, electrocatalytic, and SERS-based sensing applications. Specific studies to test this premise are currently underway.

ASSOCIATED CONTENT

Supporting Information

UV−vis absorption spectra and TEM images of the Ag NPs, representative SEM/EDS spectra and electron micrographs of the precursor Ag NSs, corresponding aerogels and xerogels, S (2p) XPS spectra and TEM images of the aerogels produced from transparent and opaque Ag hydrogels, the surface area and porosimetry plots of aerogels derived from 60.1 ± 7.6 nm outer diameter Ag NSs. This material is available free of charge via the Internet at http://pubs.acs.org.

AUTHOR INFORMATION

Corresponding Author

iuarachchige@vcu.edu

Notes

The authors declare no competing financial interest.

ACKNOWLEDGMENTS

We thank the American Chemical Society Petroleum Research Fund (Grant No. 52423-DNI10) and Virginia Commonwealth University for funding. The authors thank Lamia Nahar for high resolution SEM analysis.

REFERENCES

(1) Scher, E. C.; Manna, L.; Alivasatos, A. P. *Philos. Trans. R. Soc. London A* **2003**, *361*, 241−255.
(2) El-Sayed, M. A. *Acc. Chem. Res.* **2001**, *34*, 257−264.
(3) Murray, C. B.; Kagan, C. R.; Bawendi, M. G. *Annu. Rev. Mater. Sci.* **2000**, *30*, 545−610.
(4) Shevchenko, E. V.; Talapin, D. V.; Murray, C. B.; O'Brien, S. *J. Am. Chem. Soc.* **2006**, *128*, 3620−3637.
(5) Urban, J. J.; Talapin, D. V.; Shevchenko, E. V.; Murray, C. B. *J. Am. Chem. Soc.* **2006**, *128*, 3248−3255.
(6) Shevchenko, E. V.; Talapin, D. V.; Kotov, N. A.; O'Brian, S.; Murray, C. B. *Nature* **2006**, *439*, 55−59.
(7) Talapin, D. V.; Murray, C. B. *Science* **2005**, *310*, 86−89.
(8) Ofir, Y.; Samanta, B.; Rotello, V. M. *Chem. Soc. Rev.* **2008**, *37*, 1814−1825.
(9) Zhou, Y.; Kogiso, M.; Shimizu, T. *J. Am. Chem. Soc.* **2009**, *131*, 2456−2457.
(10) Crooks, R. M.; Zhao, M.; Sun, L.; Chechik, V.; Yeung, L. K. *Acc. Chem. Res.* **2001**, *34*, 181−190.
(11) Sreeprasad, T. S.; Samal, A. K.; Pradeep, T. *Langmuir* **2008**, *24*, 4589−4599.
(12) Wessels, J. M.; Nothofer, H.-G.; Ford, W. E.; von Wrochem, F.; Scholz, F.; Vossmeyer, T.; Schroedter, A.; Weller, H.; Yasuda, A. *J. Am. Chem. Soc.* **2004**, *126*, 3349−3356.
(13) Shavel, A.; Gaponik, N.; Eychmüller, A. *Eur. J. Inorg. Chem.* **2005**, 3613−3623.
(14) Hüsing, N.; Schubert, U. *Angew. Chem., Int. Ed.* **1998**, *37*, 22−45.
(15) Pajonk, G. M. *Catal. Today* **1997**, *35*, 319−337.
(16) Rolison, D. R. *Science* **2003**, *299*, 1698−1702.
(17) Rolison, D. R.; Dunn, B. *Chem. Rev.* **2002**, *11*, 963−980.
(18) Long, J. W.; Rolison, D. R. *Acc. Chem. Res.* **2007**, *40*, 854−862.
(19) Rolison, D. R.; Long, J. W.; Lytle, J. C.; Fischer, A. E.; Rhodes, C. P.; McEvoy, T. M.; Bourga, M. E.; Lubersa, A. M. *Chem. Soc. Rev.* **2009**, *38*, 226−252.
(20) Mahadik-Khanolkar, S.; Donthula, S.; Bang, A.; Wisner, C.; Sotiriou-Leventis, C.; Leventis, N. *Chem. Mater.* **2014**, *26*, 1318−1331.
(21) Leventis, N.; Chandrasekaran, N.; Sotiriou-Leventis, C.; Mumtaz, A. *J. Mater. Chem.* **2009**, *19*, 63−65.
(22) Leventis, N.; Chandrasekaran, N.; Sadekar, A. G.; Mulika, S. *J. Mater. Chem.* **2010**, *20*, 7456−7471.
(23) Gacoin, T.; Malier, L.; Boilot, J.-P. *Chem. Mater.* **1997**, *9*, 1502−1504.
(24) Gacoin, T.; Malier, L.; Boilot, J.-P. *J. Mater. Chem.* **1997**, *7*, 859−860.
(25) Gacoin, T.; Lahlil, K.; Larregaray, P.; Boilot, J.-P. *J. Phys. Chem. B* **2001**, *105*, 10228−10235.
(26) Mohanan, J. L.; Arachchige, I. U.; Brock, S. L. *Science* **2005**, *307*, 397−400.
(27) Arachchige, I. U.; Brock, S. L. *J. Am. Chem. Soc.* **2006**, *128*, 7964−7971.
(28) Arachchige, I. U.; Brock, S. L. *Acc. Chem. Res.* **2007**, *40*, 801−809.
(29) Hitihami-Mudiyanselage, A.; Senevirathne, K.; Brock, S. L. *ACS Nano* **2013**, *7*, 1163−1170.
(30) Bigall, N. C.; Herrmann, A.-K.; Vogel, M.; Rose, M.; Simon, P.; Carrillo-Cabrera, W.; Dorfs, D.; Kaskel, S.; Gaponik, N.; Eychmüller, A. *Angew. Chem. Int. Ed* **2009**, *48*, 9731−9734.
(31) Liu, W.; Herrmann, A.-K.; Geiger, D.; Borchardt, L.; Simon, F.; Kaskel, S.; Gaponik, N.; Eychmüller, A. *Angew. Chem., Int. Ed.* **2012**, *51*, 5743−5747.

(32) Xia, Y.; Xiong, Y. J.; Lim, B.; Skrabalak, S. E. *Angew. Chem., Int. Ed.* **2009**, *48*, 60−103.
(33) Schwartzberg, A. M.; Olson, T. Y.; Talley, C. E.; Zhang, J. Z. *J. Phys. Chem. B* **2006**, *110*, 19935−19944.
(34) Schwartzberg, A.; Zhang, J. Z. *J. Phys. Chem. C* **2008**, *112*, 10323−10337.
(35) Jackson, J. B.; Halas, N. B. *J. Phys. Chem. B* **2001**, *105*, 2743−2746.
(36) Chen, H. M.; Liu, R.-S.; Y, L. M.; Chang, S.-C.; Tsai, L.-D.; Peng, Y.-M.; Lee, J.-F. *J. Phys. Chem. C* **2008**, *112*, 7522−7526.
(37) Lee, C. L.; Tseng, C.-M.; Wu, C.-C.; Chou, T.-C.; Syu, C. M. *Nanoscale Res. Lett.* **2009**, *4*, 193−196.
(38) Guo, S.; Fang, Y.; Dong, S.; Wang, E. *J. Phys. Chem. C* **2007**, *111*, 17104−17109.
(39) Jayasayee, K.; Dam, V. A. T.; Verhoeven, T.; Celebi, S.; Bruijn, F. A. D. *J. Phys. Chem. C* **2009**, *113*, 20371−20380.
(40) Zhang, J. Z.; Noguez, C. *Plasmonics* **2008**, *3*, 127−150.
(41) Ranmohotti, K. G. S.; Gao, X.; Arachchige, I. U. *Chem. Mater.* **2013**, *25*, 3528−3534.
(42) Moshe, A. B.; Markovich, G. *Chem. Mater.* **2011**, *23*, 1239−1245.
(43) Borchert, H.; Shevchenko, E. V.; Robert, A.; Mekis, I.; Kornowski, A.; Grubel, G.; Weller, H. *Langmuir* **2005**, *21*, 1931−1936.
(44) Pattanayak, S.; Priyam, A.; Paik, P. *Dalton Trans.* **2013**, *42*, 10597−10607.
(45) Finley, J. W.; Wheeler, E. L.; Witt, S. C. *J. Agric. Food Chem.* **1981**, *29*, 404−407.
(46) Detty, M. R.; Friedman, A. E.; Oseroff, A. R. *J. Org. Chem.* **1994**, *59*, 8245−8250.
(47) Pala, I. R.; Arachchige, I. U.; Georgiev, D. G.; Brock, S. L. *Angew. Chem., Int. Ed.* **2010**, *49*, 3661−3665.
(48) Stabsbie, J. H. *J. Soc. Chem. Ind.* **1913**, *32*, 311−319.
(49) Briggs, D.; Seah, M. P. *Practical Surface Analysis: Auger and X-ray Photoelectron Spectroscopy*, 2nd ed.; Wiley and Sons: New York, 1993; Vol. *1*.
(50) Wang, J. H.; Dai, W. L.; Deng, J. F.; Wei, X. M.; Cao, Y. M.; Zhai, R. S. *Appl. Surf. Sci.* **1998**, *126*, 148−152.
(51) Zhou, W. J.; Leng, Y. H.; Hou, D. M.; Li, D. H.; Li, L. G.; Li, G. Q.; Liu, H.; Chen, S. W. *Nanoscale* **2014**, *6*, 4698−4704.
(52) Korala, L.; Brock, S. L. *J. Phys. Chem. C* **2012**, *116*, 17110−17117.
(53) Korala, L.; Li, L.; Brock, S. L. *Chem. Commun.* **2012**, *48*, 8523−8525.
(54) Webb, P. A.; Orr, C. *Analytical Methods in Fine Particle Technology*; Micromeritics: Norcross GA, 1997.
(55) Gregg, S. J.; Sing, K. S. W. *Adsorption, Surface Area and Porosity*, 2nd ed.; Academic Press: New York, 1982.